

Collaborative Framework for Robot-assisted Minimally Invasive Surgery using a 7-DoF Anthropomorphic Robot

Sandoval J.^{1*}, Hang S.², Vieyres P.³, Poisson G.⁴, Ferrigno G.⁵, De Momi E.⁶

^{1,3,4} PRISME Laboratory, University of Orleans, INSA CVL, France

^{2,5,6} Department of Electronics, Information and Bioengineering, Politecnico di Milano, Italy

Abstract— In this paper, we propose a control framework for robot-assisted minimally invasive general surgery (RA-MIS) for physical human-robot collaboration using a redundant 7-DoF serial robot. When a redundant manipulator is used in RA-MIS, the control system implemented must guarantee that the surgical tool always goes through the trocar, i.e. the medical instrument placed at the incision point on the patient's body. In addition, the redundancy of the robot can be exploited to implement a physical human-robot collaborative strategy, allowing the medical staff and robot to work in a shared common workspace without affecting the performances of the surgical task, through a null-space compliance control strategy. However, classical null-space compliance laws are defined in joint coordinates, which have some limitations. First, an arbitrary desired joint configuration is rarely contained in the robot's null-space, making the desired configuration unattainable. Moreover, the joint coordinates are not a direct representation of the robot's null-space, which limits its exploitation.

The control framework proposed in this paper is performed at the torque level. A manual motion mode is used to calibrate the trocar position before executing the task. Then, a cartesian compliance control strategy is activated during execution of the surgical task, enabling the robot to autonomously execute the surgical task while the tool orientation is calculated with respect to the trocar position. Furthermore, in order to preserve the surgical task when desired or undesired contacts occur, the null-space of the main task, i.e. surgical task, is used to implement a compliant motion in the robot's body. The compliance control approach is defined in the swivel coordinates, which effectively represent the null-space of the robot, in order to easily restrict the swivel angle motion based on joint limitations or on any other physical constraint existing in the operating room. Finally, we evaluate our control framework using a robotic system including the KUKA LWR 4+ robot, demonstrating the feasibility of the null-space compliance control approach while preserving the accuracy of the surgical task.

Keywords: Robot-assisted MIS, null-space optimization, redundant robot, compliance control

1. INTRODUCTION

In robot-assisted minimally invasive surgery (RA-MIS), a robot usually performs a surgical task, in gynecology, urology, general surgery and so on, using a tool attached to its end-effector. The surgical tool held by the robot must go inside the patient's body through a medical device, i.e. trocar, fixed at an incision cut made on the body. This kinematic constraint is commonly known as the Remote Center of Motion (RCM) constraint. In some commercialized robotic systems used for MIS, such as the Da Vinci surgical system, the kinematic design includes a fixed RCM point for each robotic arm [1]. A complete overview of mechanisms for MIS including fixed RCM designs can be found in [2] [3]. Before starting the surgical procedure, the RCM point is synchronized with the trocar position, in such a way that the surgical tool always goes through the desired incision point; then, the surgical robot can safely perform an autonomous or tele-operated task inside the patient's body. However, no specific strategy is planned to prevent degradation of the surgical task or damage to the system when collisions between the robotic arms and the environment occur.

Instead of a kinematic design with a fixed RCM point, a serial redundant robot can also be used to accomplish the surgical task, where the RCM constraint must be guaranteed by a control approach, as in the case of the MIRO robot from DLR [4]. Various studies have proposed different control approaches to effectively combine the surgical task and the RCM constraint using serial redundant manipulators [5-9]. Moreover, when using torque-controlled robots, some physical human-robot strategies can be used to allow collaborative phases during the surgical procedures, e.g. compliant motion, hands-on approaches and so on. For instance, a laparoscopic system is proposed in [10], where the robot is manually positioned in the operative workspace, i.e. a hands-on approach, and then controlled using gaze gestures. In the same way, *Cobb et al.* [11] presented in their approach a hands-on robotic device for orthopedic surgery. *Petersen et al.* [12] proposed to use a torque-controlled serial manipulator for hands-on robotic surgery, where the null-space of the Jacobian matrix is exploited to minimize the mass and frictions sensed by the surgeon.

Besides the versatility given by this type of serial systems, i.e. not only restricted to applications with a fixed incision point, the redundancy can be exploited to accomplish additional tasks, improving performance of the surgical procedure. Redundancy can be conveniently exploited to perform obstacle avoidance strategies [13], to optimize manipulability [14], and to minimize gravity torques [15] or apparent mass and friction [12]. An interesting way to exploit the redundancy of the robot is to implement a compliant motion strategy for its body. The advantage of the latter approach is that the robot and medical staff share a common workspace, even during surgery, without disturbing the surgical task. In this context, a contact may occur for various reasons. Firstly, accidental collisions may occur between the robot and the environment, e.g. staff or medical equipment. Secondly,

intentional contacts with the robot's body may be established by a member of the medical staff to modify the robot body configuration, while maintaining the desired tool pose related to the surgical task. In that case, only the robot movements in the robot's null-space are generated. Various compliance strategies applied in the null-space of the robot can be found in the literature. For instance, *Sadeghian et al.* [16] proposed a null-space compliance strategy at the acceleration level using observers to estimate the external torques. A multi-priority impedance controller without using an external force sensor at the end-effector was proposed in [17], where a higher priority level is given to the cartesian impedance control, whereas the joint impedance control is performed at a secondary level. Nevertheless, the control approaches proposed in [16] and [17] are highly dependent on the accuracy of the estimated inertia matrix. A simplified compliance control approach is proposed in [18] to avoid shaping a desired inertia matrix, using the potential function of a virtual spring and adding an appropriate damping term. This control approach was adopted in [19] to perform a null-space compliant motion, in a RA-MIS context. Moreover, most of the null-space compliance strategies found in the literature are defined in joint coordinates, where a desired joint configuration is assumed to be achieved when no external forces are applied, as in [16-17] [19]. However, an arbitrary desired joint configuration is rarely contained in the robot's null-space and therefore the compliance performance becomes hard to understand. The desired joint configuration could then be calculated in real-time in such a way that it is always contained in the robot's null-space. A main contribution of this paper is to propose another solution for this problem, consisting in the design of a compliance law using a new set of coordinates representing the robot's null-space. For instance, when using an anthropomorphic 7-DoF robot, the null-space representation can be simplified as long as the main task is defined as a cartesian 6-DoF task. The remaining degree of redundancy can be represented through an arm angle (swivel), i.e. the angle of a plane linking the robot's shoulder-elbow-wrist, measured around the axis linking the robot's shoulder and the wrist [20]. Using the swivel angle definition, *Shimizu et al.* proposed an algorithm to calculate in real-time a feasible swivel angle range based on the robot's joint limits [21]. We propose to define an intuitive null-space compliance approach using the swivel coordinates, where the compliance law can be used to constrain the null-motion in an attainable or desired swivel range of motion. Physical restrictions in the robot's workspace or its joint limits are among the choice criteria allowing the user to select this range of motion.

In this paper, we propose a complete control framework for robot-assisted minimally invasive surgery using an anthropomorphic 7-DoF robot, useful for cohabitation of the robot and medical staff in a shared workspace. In order to synchronize the trocar position with the robot, a manual motion is used allowing the medical specialist to move the tool-tip up to the incision position. Then, using a 3D camera-based system synchronized with the surgical workspace, a surgical task is commenced. The RCM constraint is accomplished by calculating the optimal tool orientation to guarantee that the incision point is always coincident to the tool axis. Furthermore, the implemented cartesian interpolator limits the velocity to ensure a safe performance. A 6-DoF cartesian compliance control task is defined as the main task. A null-space compliance task is initiated in the event of an external contact with the robot's body. The proposed strategy of using swivel coordinates restricts the null-space motion range either by restricting the workspace or by calculating a feasible null-motion range in real-time, e.g. through the algorithm proposed in [21].

The paper is organized as follows. In section II, we present the details of the proposed control framework. A real surgical procedure is proposed in section III. An experimental platform used to validate the control framework is presented in section IV and the experimental results are presented in section V. Finally, the last section provides conclusions about the control framework proposed in this paper.

2. METHODOLOGY

2.1. Surgical Task Implementation

When performing a surgical task in MIS, a tool is inserted inside the patient's body through a trocar device affixed at the surgical incision. The movement of the surgical tool is then constrained by the trocar, as shown in Fig. 1. This kinematic constraint is commonly known as the Remote Center of Motion (RCM) constraint.

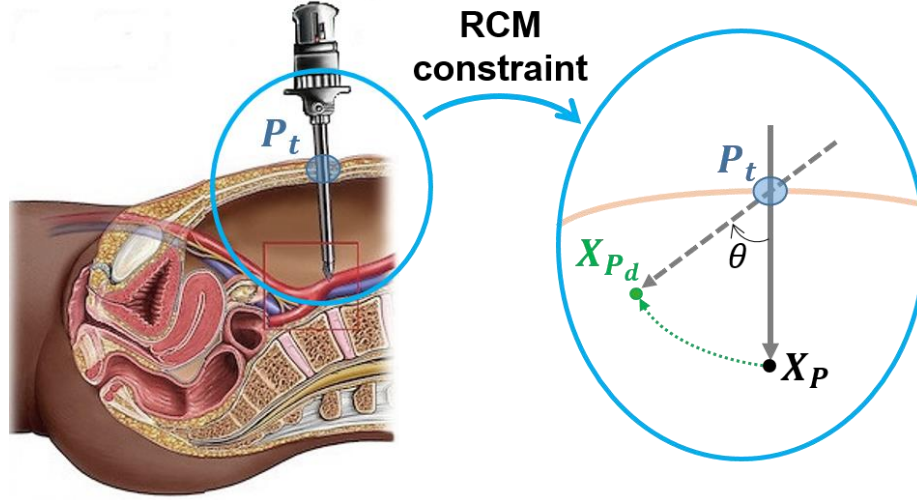


Figure 1. Surgical scene representing the RCM Constraint, i.e. the surgical tool must always go through P_t , where P_t is the 3-D trocar position, X_P and X_{P_d} are the actual and desired tool-tip positions inside the body, respectively, and θ is the angle between the actual and desired tool axis

In RA-MIS, when using a serial robot to perform a surgical task, the tool-tip trajectory and the RCM constraint must be controlled simultaneously. The operational coordinates are represented by $X = [X_P \ X_R]^T \in \mathfrak{R}^m$, with task dimension $m = 6$, where the tool-tip position $X_P \in \mathfrak{R}^3$ is given by the medical application, e.g. auto-tracking trajectory based on image recognition. Furthermore, the tool orientation $X_R \in \mathfrak{R}^3$ is calculated based on the trocar position $P_t \in \mathfrak{R}^3$, as explained below.

Given the desired cartesian position X_{P_d} , a 5th order polynomial interpolator is adopted to optimize and smooth the whole trajectory, taking into account both cartesian velocity \dot{X}_{max} and acceleration limitation \ddot{X}_{max} . Firstly, we define the distance vector $H = (H_x, H_y, H_z)$ between the actual position X_P and the desired position X_{P_d} , and the motion time T from the initial time t_0 to the final time t_f . T is not a fixed value and can be exploited as an avoidance of the limitation of \dot{X}_{max} and \ddot{X}_{max} , where:

$$\begin{cases} H = X_{P_d} - X_P \\ T = t_f - t_0 \end{cases} \quad (1)$$

Then, we define a normalized time variable ρ :

$$\rho = \frac{t-t_0}{T}, \quad 0 \leq \rho \leq 1 \quad (2)$$

where t is the current time.

It is assumed that the trajectory generated between the initial cartesian position X_{P_0} and the final cartesian position X_{P_T} fulfills the following condition:

$$\begin{cases} X_{P_0} = X_P ; X_{P_T} = X_{P_d} \\ \dot{X}_{P_0} = 0 ; \dot{X}_{P_T} = 0 \\ \ddot{X}_{P_0} = 0 ; \ddot{X}_{P_T} = 0 \\ X_t = X_{P_0} + H \cdot \sigma_\rho ; \text{where } 0 \leq \sigma_\rho \leq 1 \end{cases} \quad (3)$$

where X , \dot{X} and \ddot{X} are the cartesian position, velocity, and acceleration, respectively. σ_ρ is the normalized 5th order polynomial function defined as $\sigma_\rho = A_0 + A_1\rho + A_2\rho^2 + A_3\rho^3 + A_4\rho^4 + A_5\rho^5$. A_i ($i = 0 \dots 5$) is the constant coefficient vector calculated based on the conditions $\sigma_0 = 0, \sigma_1 = 1, \dot{\sigma}_0 = 0, \dot{\sigma}_1 = 0, \ddot{\sigma}_0 = 0, \ddot{\sigma}_1 = 0$.

Moreover, the interpolated trajectory should not exceed the cartesian velocity $\dot{X}_{max} = (\dot{x}_{max}, \dot{y}_{max}, \dot{z}_{max})$ and acceleration $\ddot{X}_{max} = (\ddot{x}_{max}, \ddot{y}_{max}, \ddot{z}_{max})$ limits. Based on the peak values of the proposed interpolator σ_ρ around each axis $\dot{x}_{max} = \frac{15H_x}{8T}$, $\dot{y}_{max} = \frac{15H_y}{8T}$, $\dot{z}_{max} = \frac{15H_z}{8T}$, $\ddot{x}_{max} = \frac{10\sqrt{3}H_x}{3T^2}$, $\ddot{y}_{max} = \frac{10\sqrt{3}H_y}{3T^2}$, $\ddot{z}_{max} = \frac{10\sqrt{3}H_z}{3T^2}$, the safest motion time can be found as the longest time, as follows,

$$T = \max \left\{ \frac{15H_x}{8\dot{x}_{max}}, \frac{15H_y}{8\dot{y}_{max}}, \frac{15H_z}{8\dot{z}_{max}}, \sqrt{\frac{10\sqrt{3}H_x}{3\ddot{x}_{max}}}, \sqrt{\frac{10\sqrt{3}H_y}{3\ddot{y}_{max}}}, \sqrt{\frac{10\sqrt{3}H_z}{3\ddot{z}_{max}}} \right\} \quad (4)$$

In order to safely guarantee the RCM constraint and to smooth the desired tool orientation trajectory during the movement, the tool orientation is updated in real-time based on the desired cartesian position X_{P_d} . Firstly, the rotation angle θ (see Fig. 1) between the actual tool direction \hat{u} and the desired tool direction $\hat{u}_d = X_{P_d} - P_t$ can be calculated as $\theta = \tan^{-1} \left(\frac{\hat{u}_d \times \hat{u}}{\hat{u}_d \cdot \hat{u}} \right)$. Moreover, the unit vector describing a rotation axis $u = [u_x \ u_y \ u_z]$ from \hat{u} to \hat{u}_d is defined by $u = \frac{\hat{u}_d \times \hat{u}}{\|\hat{u}_d \times \hat{u}\|}$. A Skew-symmetric rotation matrix $\Gamma \in \mathfrak{R}^{3 \times 3}$ is given by:

$$\Gamma = \begin{pmatrix} 0 & -u_z & u_y \\ u_z & 0 & -u_x \\ -u_y & u_x & 0 \end{pmatrix} \quad (5)$$

Finally, the desired orientation can be calculated using:

$$R_d = (I + \Gamma \sin \theta + 2\Gamma^2 \sin^2 \frac{\theta}{2}) \cdot R \quad (6)$$

where R and R_d are the actual and desired rotation matrix, respectively.

2.2. Modeling of the Manipulator

The control approach is proposed to be applied in torque-controlled robots. The joint dynamic model of a n -DoF serial manipulator in the Lagrangian formulation is expressed as:

$$M(q)\ddot{q} + C(q, \dot{q})\dot{q} + g(q) = \tau_c - \tau_{EXT} \quad (7)$$

where $M(q) \in \mathfrak{R}^{n \times n}$ is the inertia matrix, $C(q, \dot{q}) \in \mathfrak{R}^n$ is a matrix representing the Coriolis and Centrifugal effects, and $g(q) \in \mathfrak{R}^n$ is the gravity torque vector. The torque $\tau_c \in \mathfrak{R}^n$ is the control torque vector and $\tau_{EXT} \in \mathfrak{R}^n$ contains the external torques acting on the robot's body, i.e. due to contacts with the environment or to physical human-robot interaction.

Assuming that the robot is provided with external torque sensors to measure $\hat{\tau}_{EXT} \in \mathfrak{R}^n$, and estimating the compensation torques $\hat{C}(q, \dot{q}) \in \mathfrak{R}^n$ and $\hat{g}(q) \in \mathfrak{R}^n$, a well-known control solution $\tau_c \in \mathfrak{R}^n$ [22] can be defined as follows:

$$\tau_c = \tau_T + \tau_N + \hat{C}(q, \dot{q})\dot{q} + \hat{g}(q) + \hat{\tau}_{EXT} \quad (8)$$

where $\tau_T \in \mathfrak{R}^n$ is the control torque signal implementing the main task, i.e. the surgical task. Moreover, a second control torque signal $\tau_N \in \mathfrak{R}^n$ implements additional tasks in the null-space of the main task.

In order to perform the surgical task presented in the previous section, we propose to use a compliance control strategy based on the definition of the potential function of a virtual spring and added to a damping term, as used in [18], given by:

$$\tau_T = J^T F_T = J^T \left(\left(\frac{\partial P(X_e)}{\partial X} \right)^T - D_x \dot{X} \right) \quad (9)$$

where $D_x \in \mathfrak{R}^{m \times m}$ is a positive definite diagonal matrix corresponding to the damping parameter. Moreover, the virtual potential function $P(X_e)$ is defined as a function of the difference between the desired and the actual cartesian trajectory $X_e(q) = X_d - X(q)$, as follows:

$$P(X_e(q)) = \frac{1}{2} X_e(q)^T K_x X_e(q) \quad (10)$$

where $K_x \in \mathfrak{R}^{m \times m}$ is a positive definite diagonal matrix corresponding to the stiffness parameter in the compliance law.

In the next section, we propose a null-space compliance motion strategy to deal with desired or undesired physical interactions with the robot's body during the surgical procedure.

2.3. Null-space Compliance Strategy

The control torque solution proposed in Eq. (8) allows the implementation of additional tasks aside from the surgical task, by using the null-space projected control torque τ_N . In order to guarantee a higher priority of the surgical task τ_T over a secondary task, a strict hierarchy projection can be applied. In this type of strictness, a higher priority level task is decoupled from the lower level task. This means that the lower priority task is performed as well as possible without disturbing the performances of the higher priority task. The null-space projected task can then be defined as:

$$\tau_N = N\tau_S = [I - J(q)^T (J(q)_W^+)^T] \tau_S \quad (11)$$

where $N \in \mathfrak{R}^{n \times n}$ represents the null-space projector. $J(q)_W^+ \in \mathfrak{R}^{n \times m}$ is the weighted generalized inverse denoted by $J(q)_W^+ = W^{-1} J^T (JW^{-1} J^T)^{-1}$, where $W \in \mathfrak{R}^{n \times n}$ is a symmetric positive definite matrix. The control torque $\tau_S \in \mathfrak{R}^n$ represents a secondary task. In order to guarantee a dynamic consistency property, i.e. no interference between the hierarchic levels in the transient and steady state, the weighted generalized inverse is calculated using $W = M(q)$, resulting in the inertia-weighted pseudo-inverse $J(q)_M^+ \in \mathfrak{R}^{n \times m}$ [22].

In order to simultaneously accomplish the surgical task and a compliant motion in the robot's body, the null-space of the robot can be used to perform a compliance task while preserving the surgical task during physical contacts with the robot's body.

As mentioned above, the surgical task dimension is $m = 6$, related to the 6-DoF needed to control the tool pose. In the case of an anthropomorphic 7-DoF serial robot, the degree of redundancy, denoted by $r = n - m = 7 - 6 = 1$, can be easily represented as an arm angle $\psi \in \mathfrak{R}$ measured around the axis \overline{SW} defined between the robot's shoulder and wrist, as shown in Fig. 2. Making use of geometric relations, the arm angle, commonly known as *swivel angle*, can be calculated by:

$$\Psi = \text{sgn} \left((\overline{BS} \times \overline{SE}) \cdot \overline{SW} \right) \cos^{-1} \left(\frac{(\overline{BS} \times \overline{SW}) \cdot (\overline{SE} \times \overline{EW})}{\|\overline{BS} \times \overline{SW}\| \|\overline{SE} \times \overline{EW}\|} \right) \quad (12)$$

where \overline{BS} is the vector from the robot's base to the shoulder, \overline{SE} is the vector from the robot's shoulder to the elbow, \overline{SW} is the vector from the robot's shoulder to the wrist and \overline{EW} is the vector from the robot's elbow to the wrist. Naturally, even if the range of Ψ is $[-\pi, \pi]$, not all the swivel angles can be reached due to the joint range limitations. An optimal formulation of the real-time calculation of the feasible motion range, taken from [21] is used in this paper.

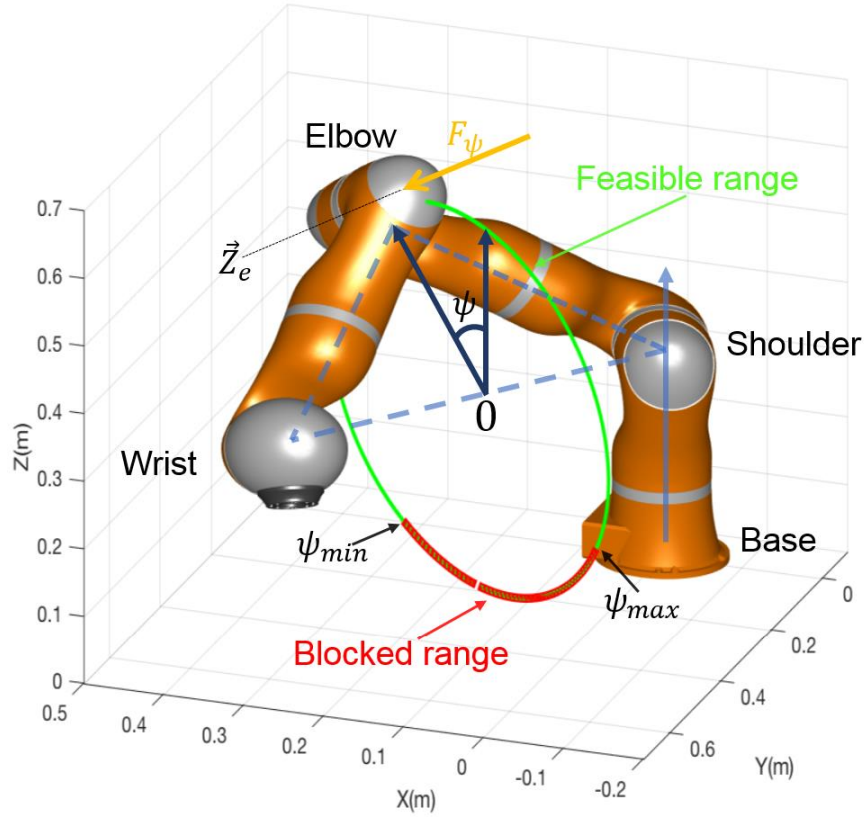


Figure 2. Redundancy representation of a 7-DoF serial robot. The swivel angle ψ is defined as the angle between the reference plane (Base-Shoulder-Wrist) and the actual arm plane (Shoulder-Elbow-Wrist). Its total range is $[-\pi, \pi]$ and it can be divided in two parts: a feasible swivel angle range and a blocked unachievable range due to joint range limitations or due to constraints in the robot's workspace. When activating the null-space compliance in the swivel coordinates, the virtual force F_ψ is applied along the elbow joint axis \vec{Z}_e to constrain the swivel motion

Furthermore, an optimal compliance motion strategy should limit the null-motion based on the feasible swivel angle range. The swivel motion can also be constrained by physical objects placed inside the robot's workspace. Thus, the compliance strategy should constrain the swivel motion either from the limits of the feasible swivel angle or from limits given by constraints in the robot's workspace.

As explained above, unlike previous studies proposing null-space compliance approaches defined in joint coordinates, we propose to determine a compliance law using the swivel coordinates. This definition enables the compliance to be directly controlled in terms of the actual swivel angle ψ and the swivel motion limits $\psi_{min}, \psi_{max} \in \mathfrak{R}$. A virtual force $F_\psi \in \mathfrak{R}^{3 \times 1}$ can then be designed to implement the compliance law. In order to effectively control the swivel motion, the virtual force F_ψ is applied at the robot's elbow, along its joint axis \vec{Z}_e . Therefore, the secondary task τ_s from Eq. (11) can be defined as:

$$\tau_s = \left[(J_e^T F_\psi)^T \quad 0 \quad 0 \quad 0 \right]^T - \hat{\tau}_{EXT} \quad (13)$$

where $J_e \in \mathfrak{R}^{3 \times 4}$ is the Jacobian elbow matrix mapping the joint velocities to the robot's elbow velocities. From the control solution defined in Eq. (8), it can be observed that the external torques are compensated through the measured external torques $\hat{\tau}_{EXT}$, in such a way that the surgical task is not disturbed by the external torques applied to the robot's body. Nevertheless, although the external torques should be compensated for the surgical task, the null-motion in the secondary task is actually launched by the external torques acting on the robot's body. Hence, the measured external torques $\hat{\tau}_{EXT}$ are included in the secondary task defined in Eq. (13).

When the external forces are applied to the robot's body, the swivel motion is freely allowed as long as the swivel angle ψ remains within the feasible range. Once one of the swivel motion limits ψ_{min}, ψ_{max} is reached, the compliance law is activated to constrain the swivel motion. The virtual force F_ψ applied along \vec{Z}_e reproduces a damper-spring system behaviour, and is defined as follows:

$$F_\psi = [0 \quad 0 \quad F_{\psi_z}]^T \rightarrow F_{\psi_z} = \begin{cases} k_\psi(\psi_{min} - \psi) - d_\psi\dot{\psi} & \text{if } \psi \leq \psi_{min} \\ k_\psi(\psi_{max} - \psi) - d_\psi\dot{\psi} & \text{if } \psi \geq \psi_{max} \\ 0 & \text{if } \psi_{min} < \psi < \psi_{max} \end{cases} \quad (14)$$

where $k_\psi \in \mathfrak{R}$ and $d_\psi \in \mathfrak{R}$ are the positive stiffness and damping constants, respectively.

The block diagram shown in Fig. 3 represents the proposed control architecture. An *auto-tracking generator* block is in charge of producing the desired reference tool-tip trajectory X_{Pd} according to the surgical procedure to be performed. Based on X_{Pd} and on the trocar position P_t , the polynomial interpolator presented in section 2.1 calculates the desired trajectory in operational coordinates X_d . The control torque τ_T implementing the surgical task and the control torque τ_N related to the null-space compliance controller compose the overall control torque τ_C sent to the robot, which is completed by the compensation torques of the dynamic effects, i.e. centrifugal, Coriolis and gravitational effects, as well as the estimated external torques $\hat{\tau}_{EXT}$.

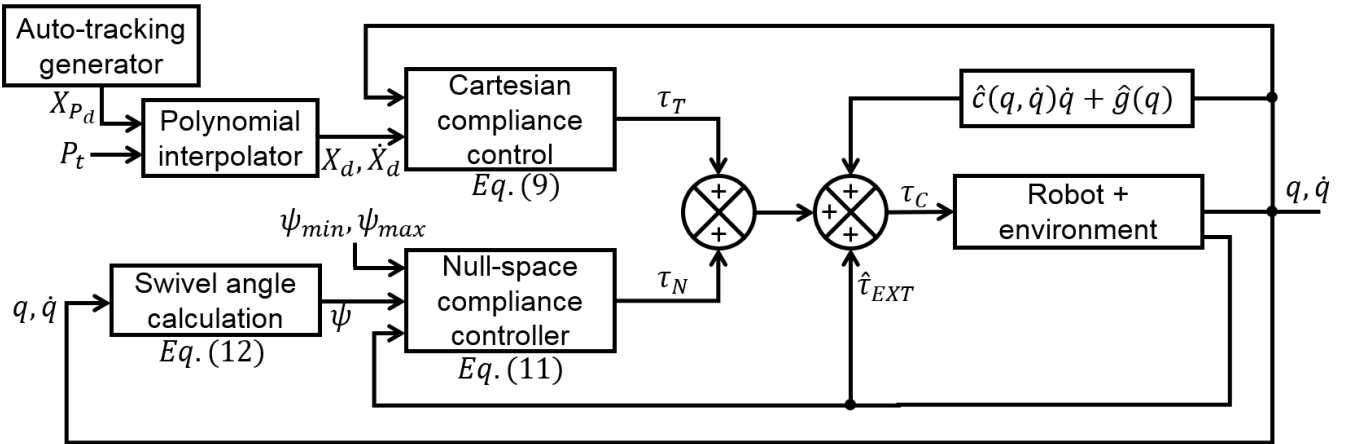


Figure 3. Block diagram representing the proposed control architecture. The control torque τ_C is composed of the centrifugal, coriolis and gravitational compensation torques, the measured external torques $\hat{\tau}_{EXT}$ as well as the control torques τ_T and τ_N related to the surgical task and the null-space compliance task, respectively

3. PLATFORM SETUP PROCEDURE

In this section, we propose a setup procedure to launch the surgical platform. The procedure is composed of two sequential steps: “pre-operative” and “operative” steps, as shown in Fig. 4. During the pre-operative step, the robot is synchronized with the trocar position, where the surgical tool is going to be inserted inside the patient's body. A manual motion mode is activated allowing the user to freely move the robot by hand. This motion mode is easily activated by setting the control torque signal as $\tau_C = \hat{C}(q, \dot{q})\dot{q} + \hat{g}(q)$. Then, the user manually moves the robot tool to the trocar position so that the tool-tip coincides exactly with the incision position. In order to set the trocar position coordinates P_t in the robot's reference frame (base frame), we use the forward kinematics of the robot to calculate and record the tool-tip position which temporarily coincides with the incision point. Once this recording phase done, the trocar position P_t can be used by the controller since it is henceforth known by the robot.

Once the desired incision position has been set in the controller, the pre-operative step is completed. Subsequently, the operative step starts, by switching to the control torque input defined in Eq. (8). As shown at the right-side of Fig. 4, the surgical tool autonomously follows a desired trajectory X_{Pd} while the tool orientation is calculated in such a way that the tool axis always goes through the trocar position P_t .

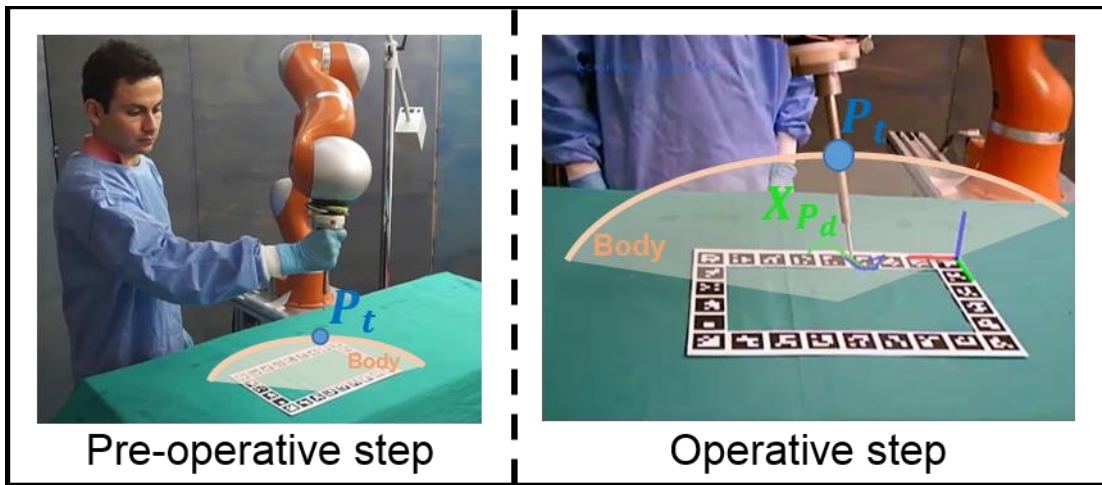
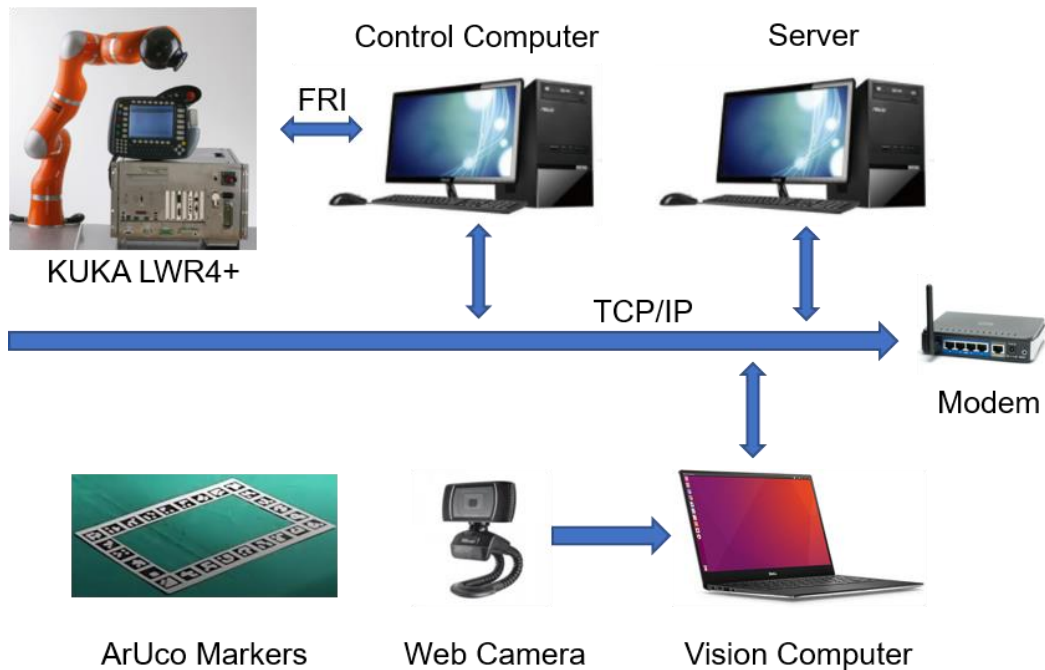


Figure 4. The setup procedure is divided in two sequential steps: pre-operative and operative steps. First, during the pre-operative step, the user manually moves the surgical tool-tip up to the incision position where the trocar device is placed, synchronizing P_t in the controller. Then, the operative step begins by activating the controller of Fig. 3, starting the surgical procedure

4. MATERIAL

In this section, we present in detail the material used to develop the proposed robotic platform, including a detailed data flow between the different components composing the robotic framework. In Fig. 5, we present an overview of the system. The autonomous control system was developed based on the OROCOS¹ framework, using a computer running Ubuntu² 12.04 with the Xenomai³ real-time kernel patch, and ROS⁴ kinetic, installed on a computer running Ubuntu 16.04. A ROS vision node, previously presented in [23], was implemented to provide the user with visual feedback, whereas the torque controller was developed on an OROCOS component. Both the ROS vision node and the torque controller were executed on separate computers, the Control Computer and the Vision Computer, respectively, and connected via UDP communication. The control loop was developed in C++ and executed on the Control Computer, whereas the ROS vision node, executed on the Vision Computer, was developed in C++ using the OpenCV library.



¹ <http://www.oroocos.org/>

² <http://www.ubuntu.com/>

³ <http://www.xenomai.org/>

⁴ <http://www.ros.org/>

Figure 5. Overview of the autonomous surgical robot system: the system includes a KUKA LWR 4+ redundant robot utilized as the surgical robot, a 720p webcam (30 fps) providing visual feedback of the surgical task execution, and an ArUco marker board employed to define a visual task inside the robot’s workspace [22]

4.1. Communication framework

The communication rates between the ROS node and the OROCOS components are shown in Fig. 6. It can be seen that the communication frequency between the robot’s controller and the control computer is around 500Hz, as recommended for torque-controlled implementations using the Kuka LWR4+ robot [25]. The vision node working rate was set to 30 Hz. The trajectories related to the surgical tasks are generated on the vision computer and sent to the Trajectory generator component to calculate the desired tool pose.

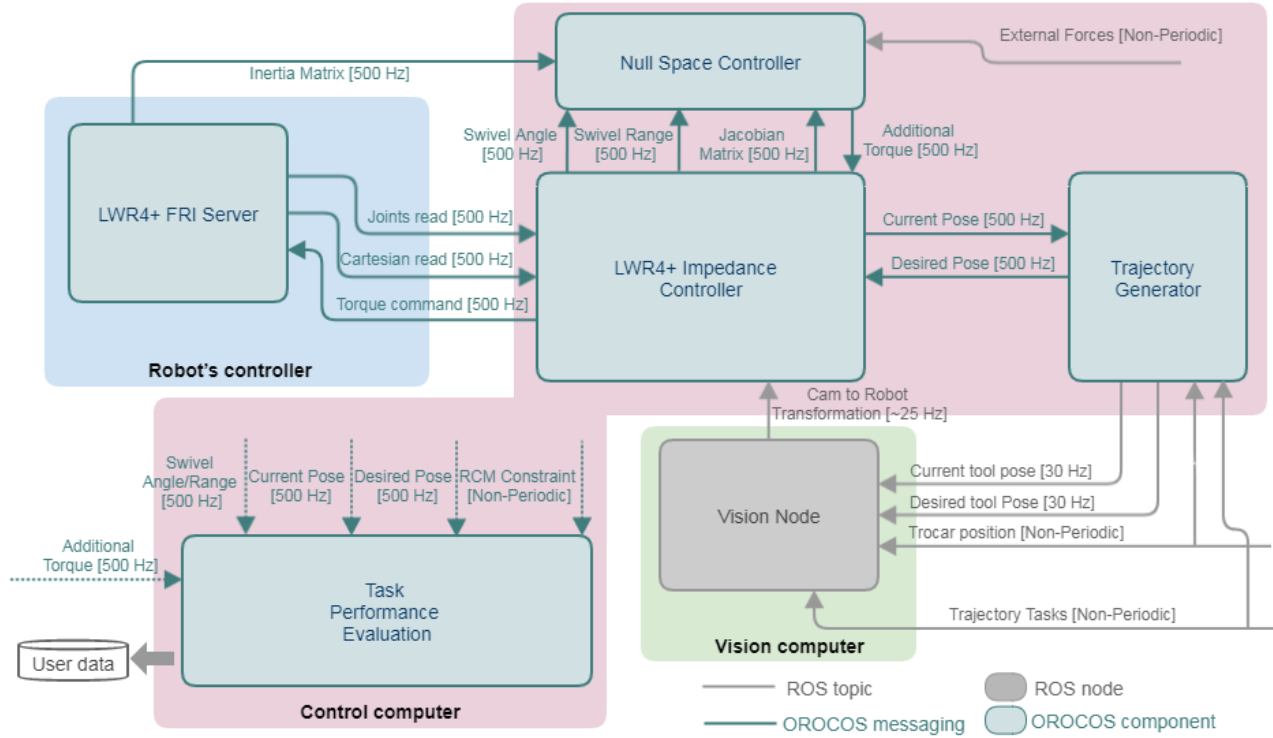


Figure 6. Data flow diagram for the control framework implemented around the Kuka LWR 4+ robot, based on OROCOS and ROS middlewares: the LWR4+ FRI Server component is in charge of the data transfer between the remote user’s computer, i.e. Control computer, and the robot’s controller; the trajectory generator component is used to generate in real-time the desired tool pose; the LWR4+ impedance control component implements the compliance control related to the desired tool pose, whereas the null-space controller component implements the null-space compliance control. Finally, the vision node, previously presented in [23], allows one to follow in real-time the surgical procedure through a visual feedback

The Fast Research Interface (FRI), developed by KUKA, provides direct real-time access to the robot’s controller at high rates of up to 1 kHz [25], making it possible to implement control torque strategies, e.g. compliance control approaches. Moreover, each robot joint is equipped with a torque sensor to measure the external forces acting on the robot. As explained above, the robot joint limitations are used to calculate in real-time the feasible swivel angle range. We used the robot joint limitations given by the constructor: $[\pm 170^\circ, \pm 120^\circ, \pm 170^\circ, \pm 120^\circ, \pm 170^\circ, \pm 120^\circ, \pm 170^\circ]$. The cartesian velocity and acceleration limitations are fixed to $\dot{X}_{max} = 0.3$ m/s and $\ddot{X}_{max} = 0.3$ m/s², respectively.

4.2. Vision System

The vision feedback trajectory task is achieved through the synchronization between the RGB web camera and the ArUco marker board. The web camera provides 1280×720 pixels in 8-bit per channel, delivering the three basic color components. The markers are attached to the operating table and are detected with high precision by the camera, based on the OpenCV ArUco library [24].

The visual feedback developed on the vision node provides the camera image in real-time, the trocar position, the desired trajectory task and the current tool-tip position. The transformation from the task reference frame to the robot’s reference frame is estimated through a calibration process. The task is then related to the marker board, with no influence on the camera’s position.

Figure 7 shows a representation of a surgical scene during the operative step. In a real scenario, the marker board would be associated to the patient’s body, in such a way that the trajectory task can be generated relative to the patient’s body and according to the type of surgical procedure. Once the marker board and camera have been synchronized and the trajectory task defined, the robot starts to follow the trajectory while preserving the RCM constraint generated by the trocar position. The visual feedback

for three different trajectory tasks is shown on the bottom of Fig. 7, where the trocar position P_t as well as the desired (green line) and actual (blue line) trajectories, X_{P_d} and X_P respectively, are displayed. The three trajectory tasks shown in Fig. 7 (semicircle, “S” and triangle, respectively) exemplify that there is no restriction on the shape of the trajectory performed by the tool-tip. Moreover, during execution of the task, a medical operator exerts force on the robot body, changing the null-space configuration, as shown at the top of Fig. 7.

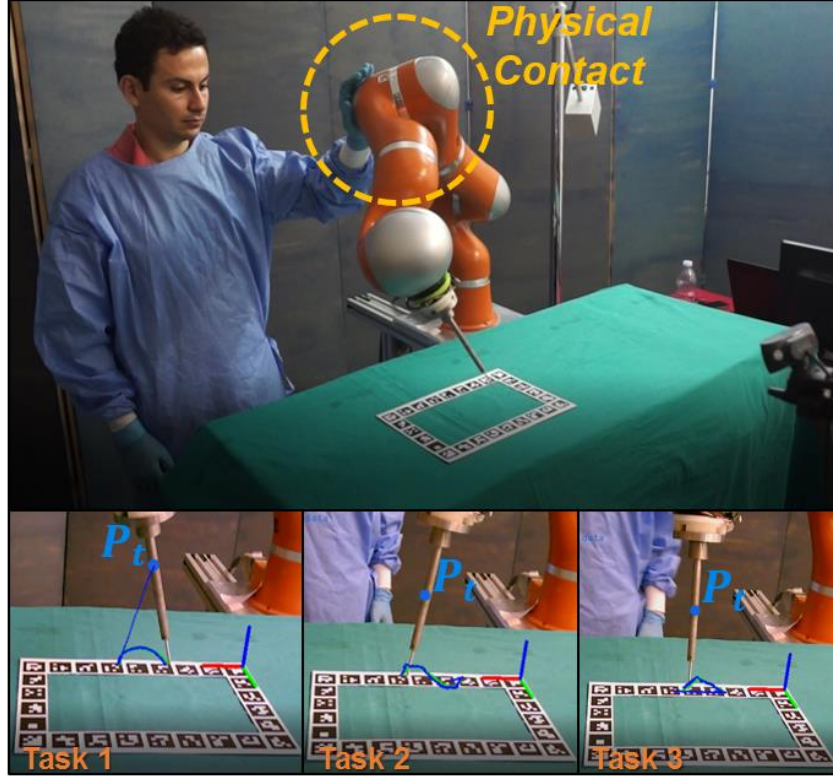


Figure 7. Representation of a surgical scenario. Top: During the surgical procedure, a desired or undesired contact occurs with the robot body. Bottom: visual feedback providing the trocar position P_t , the desired trajectory X_{P_d} (green line) and the actual trajectory X_P (blue line). Three different tasks are performed by the surgical tool-tip

5. EXPERIMENTAL RESULTS

In this section we present some experimental results obtained with the robotic system presented in section 4. Two experiments are presented to validate the effectiveness of the proposed collaborative control framework. In the first experiment we validate the proposed null-space compliance controller. A medical operator manually changes the null-space configuration, i.e. the swivel angle, while the robot keeps a constant desired surgical tool pose. In the second experiment, the performances of both tasks, i.e. the surgical task and the null-space compliance task, are simultaneously evaluated. That is, the surgical tool-tip follows a generated trajectory while the RCM constraint is preserved by the controller. Simultaneously, a medical operator contacts with the robot body to change the null-space configuration. In both experiments, the performance of the null-space compliance controller is verified when the swivel motion reaches its limits. It is worth mentioning that the algorithm presented in [21] was used to calculate the swivel motion range limits $[\psi_{min}, \psi_{max}]$. However, since these limits are calculated based on the joint range limitations, their use as a reference swivel position to activate the compliance law can cause damage to the robot joints. The compliance law is then activated once the swivel angle reaches one of the constant swivel motion range limits $[\psi_{minf}, \psi_{maxf}]$, where $\psi_{minf} > \psi_{min}$ and $\psi_{maxf} < \psi_{max}$. Furthermore, the compliance parameters were set to $K_x = \text{diag}\{3000, 3000, 3000, 300, 300, 300\}$ N/m, $D_x = \text{diag}\{30, 30, 30, 3.5, 3.5, 3.5\}$ Ns/m, $k_\psi = 150$ N/rad and $d_\psi = 5$ Nrad/s.

5.1. First experiment: null-space compliance controller

In this experiment, we verify the performance of the null-space compliance strategy when the surgical tool maintains a fixed desired position and orientation, X_{P_d} and X_{R_d} respectively. In the first part of the experiment, while $time < 105$ s, the null-space compliance control strategy is applied, constraining the swivel motion once the swivel range limits $[\psi_{minf}, \psi_{maxf}]$ are exceeded. In a second stage, when $time > 105$ s, the compliance law is deactivated, i.e. $F_{\psi_z} = 0$, and the medical operator is able to freely modify the null-space configuration, even exceeding the limits $[\psi_{minf}, \psi_{maxf}]$. We set $X_{P_d} = \{-0.46, 0.38, 0.11\}$ m and $X_{R_d} = \{-2.95, 0.03, 0.36\}$ rad as the desired tool-tip position and tool orientation, respectively. Figure 8 shows the swivel motion behaviour during the experience. The experiment starts with the swivel angle in the

unconstrained range, i.e. $\psi_{minf} < \psi < \psi_{maxf}$. At the *time* ≈ 48 s, the medical operator touches the robot body, near the elbow, modifying the null-space configuration, as verified in Fig. 8 with the variation of the swivel angle value. The control solution defined in Eq. (8) actually acts in such a way that the external torques applied by the operator are compensated through the measured external torques $\hat{\tau}_{EXT}$, in order to preserve the main task. Then, these measured torques are projected in the null-space through Eq. (13). In this way, the influence of the external forces applied by the operator is exclusively restricted to the null-space behaviour.

Fig. 9 shows the evolution of the virtual force F_{ψ_z} applied along the elbow joint axis \hat{Z}_e . As defined in Eq. (14), the force is activated once one of the swivel range limits has been reached, constraining the medical operator's intention. Comparing figures 8 and 9, it can be verified that the magnitude of the virtual force increases when the medical operator tries to exceed the range limits, as evidenced in Fig. 9 through the peaks generated in the F_{ψ_z} signal. It is worth mentioning that the response of the null-space compliance control is accomplished in real-time, as can be seen in Fig. 8 and 9, where the virtual force F_{ψ_z} is immediately activated once one of the swivel range limits has been reached. The increase in the magnitude of the virtual force F_{ψ_z} , acting in the opposite direction to the force applied by the medical operator, restricts the swivel motion through a complaint behaviour. In the interval time from 66 to 78 s, the medical operator stops the contact with the robot body. According to the compliance behaviour, the swivel angle should immediately recover its equilibrium position, i.e. the exceeded limit ψ_{minf} , but the swivel angle stabilizes at a constant value different from ψ_{minf} , generating a residual constant virtual force $F_{\psi_z} \neq 0$. This phenomenon can be caused by joint frictions, which have higher magnitudes than the additional torques generated by the compliance task τ_N , or by a residual error associated to the accuracy of the dynamic robot model used to compensate the centrifugal, Coriolis and gravitational effects, i.e. $\hat{C}(q, \dot{q})$ and $\hat{g}(q)$; in our case, these compensation torques are directly calculated by the robot's controller. Nevertheless, further analysis and experiments should be performed to fix this phenomenon.

Figure 10 shows the cartesian position error X_{Pe} , defined as the difference between the desired and the actual cartesian tool-tip position, i.e. $X_{Pe} = X_{Pd} - X_P$.

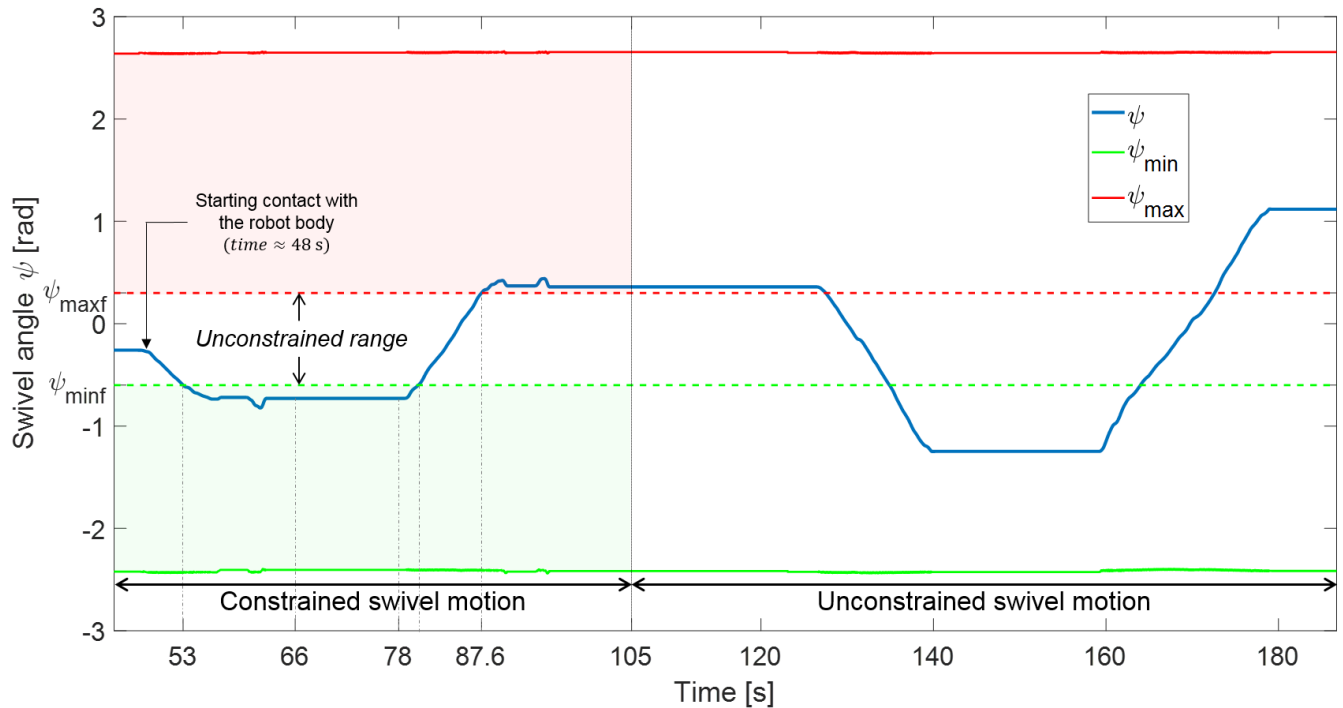


Figure 8. First experiment. Swivel angle ψ behaviour for a fixed cartesian pose $[X_{Pd} \ X_{Rd}]^T$

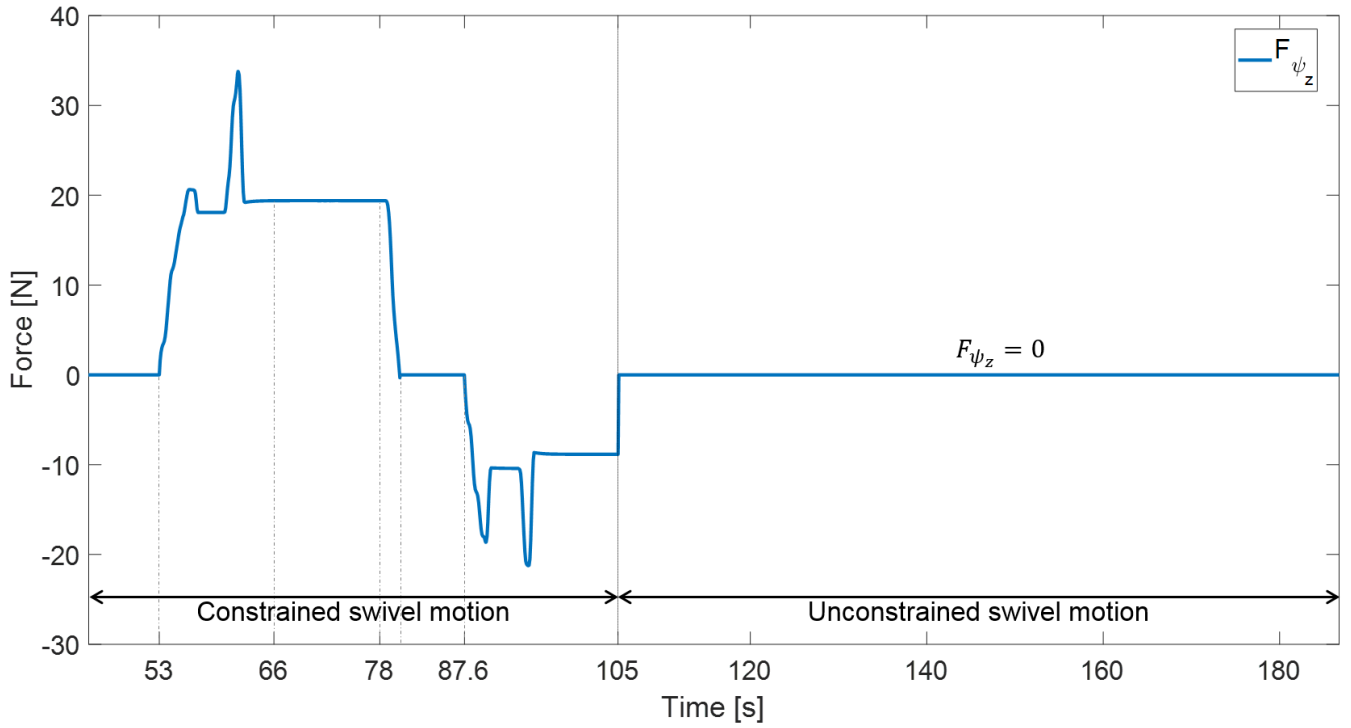


Figure 9. First experiment. Virtual force F_{ψ_z} projected in the null-space of the surgical task to constrain the null-space motion once the swivel range limits $[\psi_{min}, \psi_{max}]$ have been exceeded

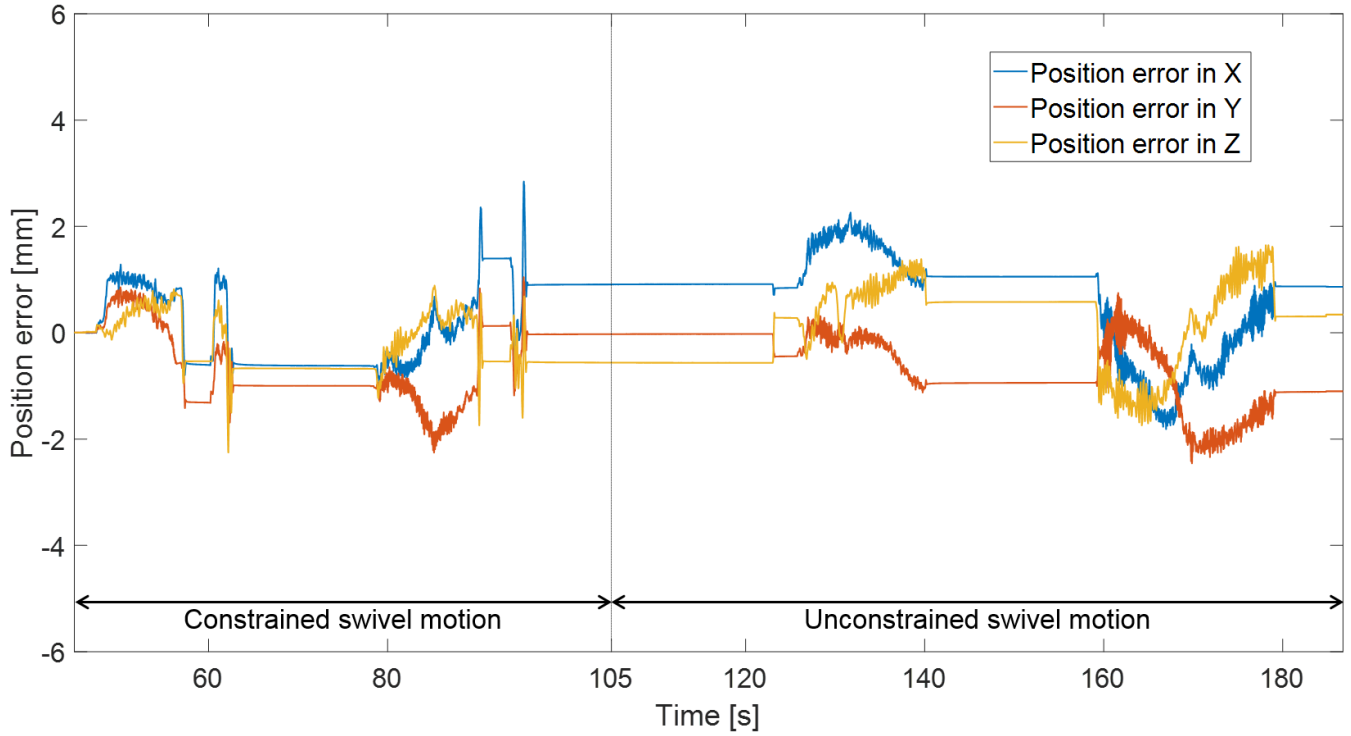


Figure 10. First experiment. Cartesian position error X_{P_e} calculated as the difference between the desired X_{P_d} and the actual X_P cartesian tool-tip position

In order to evaluate the accuracy of the cartesian compliance task, the root-mean-square error (RMSE) of the cartesian tool-tip position $RMSE_{\lambda_{X_P}}$ was calculated as follows:

$$RMSE_{\lambda_{X_P}} = \sqrt{\frac{\sum_{i=1}^k \|X_{P_i} - X_{P_{di}}\|^2}{k}} \quad (15)$$

where k is the number of data points collected, whereas $X_{P_{di}}$ and X_{P_i} are the i^{th} desired and actual cartesian position, respectively. The $RMSE_{\lambda_{X_p}}$ was calculated separately for the two interval times discriminated during the experiment, i.e. while the null-space compliance strategy was activated (until $time = 105$ s) and then when it was deactivated (from $time = 105$ s), as presented in Table I.

TABLE I
RMSE PERFORMANCE EVALUATION

Interval time	Null-space compliance task state	$RMSE_{\lambda_{X_p}}$ (mm)
$time < 105$ s	Activated	1.7
$time > 105$ s	Deactivated	1.3

Root-mean-square error (RMSE) related to the cartesian position accuracy for the first experiment

5.2. Second experiment: RCM constraint performance verification

In the second experiment, we verify the performance of both tasks, the surgical task and the null-space compliance task. Unlike the first experiment, the null-space compliance control strategy is always applied, constraining the swivel motion once the swivel range limits $[\psi_{minf}, \psi_{maxf}]$ have been exceeded. In this case, the three different 3-D task curves shown in Fig. 7 are generated by the vision node and performed by the surgical tool-tip. During the execution of the surgical tasks, the medical operator moves the robot's elbow from the unconstrained range until reaching the swivel range limits $[\psi_{minf}, \psi_{maxf}]$. The experimental results shown in Fig. 11-14 correspond to the first 3-D task generated. Similar results were found for the second and third 3-D tasks, as displayed in Fig. 15, however, their detailed description are omitted here for brevity's sake. Figure 11 shows the swivel motion behaviour during the experiment. Likewise, Fig. 12 presents the virtual force F_{ψ_z} applied along the elbow joint axis \hat{Z}_e . Similar to the first experiment, the swivel angle value begins the experiment in the unconstrained range, i.e. $\psi_{minf} < \psi < \psi_{maxf}$. Then, the medical operator moves the robot body, modifying the null-space configuration. During the experiment, the swivel range limits are exceeded in two interval times. First, while $79.2 \text{ s} \leq time \leq 138.5 \text{ s}$, the limit ψ_{minf} is exceeded, generating a positive virtual force F_{ψ_z} blocking the operator's intention. Likewise, the limit ψ_{maxf} is exceeded during $160.8 \text{ s} \leq time \leq 182.6 \text{ s}$, producing a negative force F_{ψ_z} , as shown in Fig. 12.

A further point to consider is the effectiveness of the virtual force F_{ψ} designed to restrain the swivel motion. We applied the virtual force F_{ψ} to the center of the elbow, always normal to the plane linking the robot's shoulder-elbow-wrist (Figure 2). This option was chosen because only the normal component of a force applied to the elbow is able to move the arm around the shoulder-wrist axis, i.e. the tangential component of the force generates no leverage. Furthermore, the choice of the center of the elbow as the point of application of F_{ψ} is justified by the fact that this is the farthest point from the shoulder-wrist axis in the robot body, so a minimal input force is needed to generate a movement around the axis. On the other hand, it is important to point out that our proposed control approach does not require any identification of the contact position with the environment on the robot body. Nevertheless, its identification could improve the compliance strategy when the swivel range limits are exceeded, since in that case the virtual force F_{ψ} could be applied at the same position as the contact, with the same orientation as the external force but in the opposite direction.

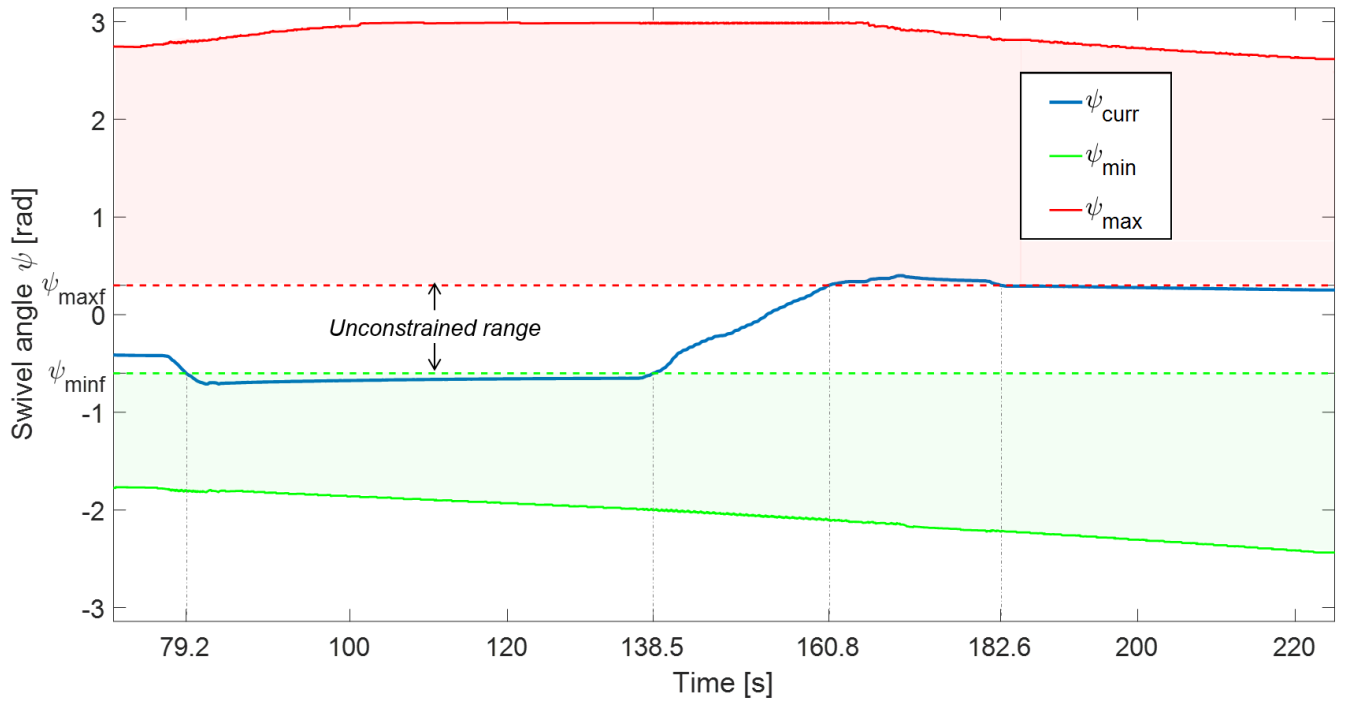


Figure 11. Second experiment (first 3-D task). Swivel angle ψ behaviour during the tracking of a desired cartesian trajectory $X_{p_d}(t)$. A medical operator establishes contact with the robot's elbow to change the value of ψ . The null-space compliance strategy restricts the swivel motion to an unconstrained range delimited by $[\psi_{minf}, \psi_{maxf}]$

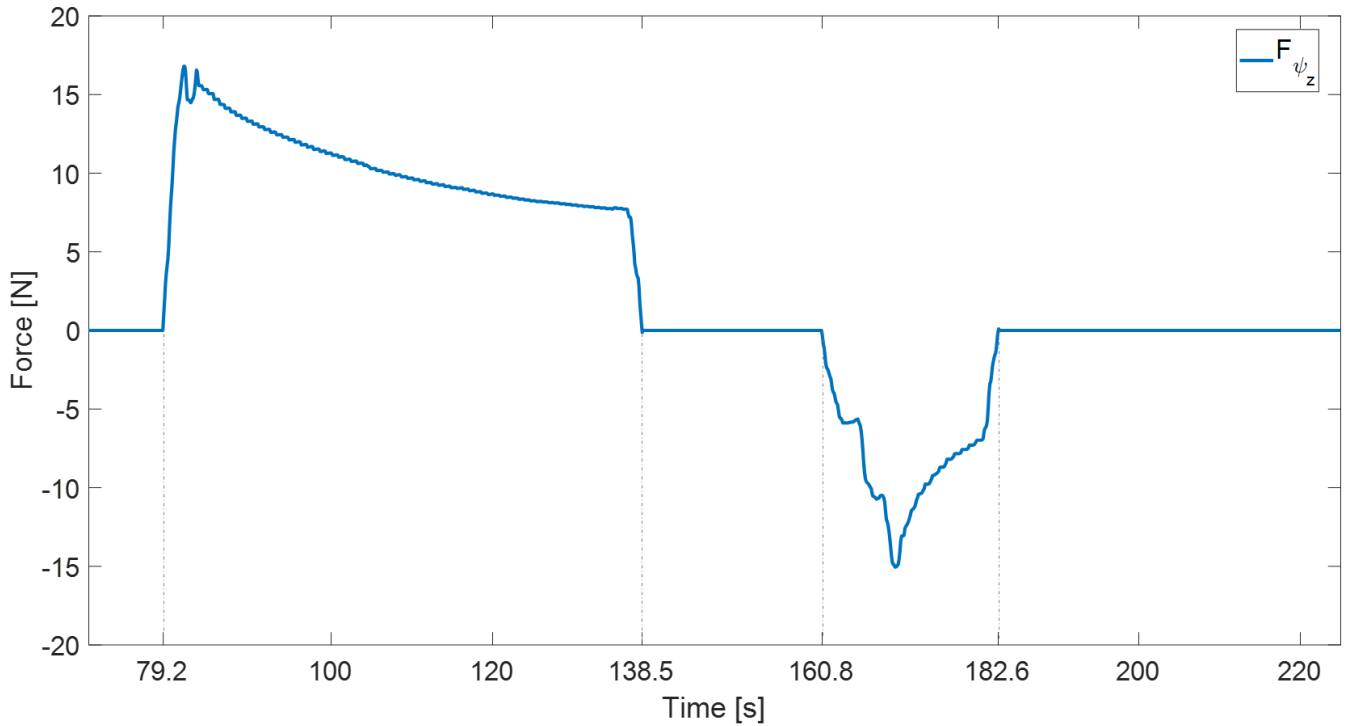


Figure 12. Second experiment (first 3-D task). Virtual force F_{ψ_z} projected in the null-space of the surgical task to constrain the null-space motion once the swivel range limits $[\psi_{minf}, \psi_{maxf}]$ have been exceeded

Furthermore, Figures 13 and 14 show the cartesian position and RCM constraint errors, X_{p_e} and E_{p_t} respectively. The RCM constraint error E_{p_t} is calculated as the minimal distance between the trocar position P_t and the current surgical tool axis \vec{u}_c , as follows:

$$E_{p_t} = \|(P_t - X_p) \times \hat{u}_c\| \quad (16)$$

where \hat{u}_c is the unit vector of the current tool axis \vec{u}_c .

We noted that the maximum cartesian position error X_{p_e} is around 2 mm. The RCM constraint error is within 6 mm. These error values have a similar order of magnitude compared with those found in previous studies [7-9]. The main difference with the studies cited in [7-9] is that no null-space compliance strategy was implemented in those studies. It means that the proposed control approach guarantees the dynamic consistency property, i.e. there is no interference of the null-space task on the main task (tool pose), which was one of the most important issues in the design of the control strategy. Furthermore, it is worth mentioning that the cartesian position and RCM constraint errors are also dependent on the compliance parameters set in the control tasks, so the tool compliance can be adapted according to the specific application needs.

The goal of the proposed null-space control approach is to allow the user to restrain the swivel motion within a feasible range through an intuitive control formulation, where the user is able to define the swivel range limits. Moreover, the swivel angle coordinate is a natural measure that enables the user to easily recognize the actual arm configuration, even for regular users without any specific knowledge of robot kinematics. This approach cannot be easily compared with classical null-space compliance control approaches defined in joint coordinates, e.g. [16-17] [19], however, since these type of approaches do not include an intuitive way to define a swivel range. They typically define a virtual joint position vector $q_d \in \mathcal{R}^n$ to coerce the robot to keep this virtual position, which is not necessarily included in the robot's null-space, i.e. only a limited number of q_d values can in fact be reached. This is why the use of the swivel coordinates represents an advantage to define the null-space compliance law, since the swivel angle is a direct representation of the values contained in the robot's null-space.

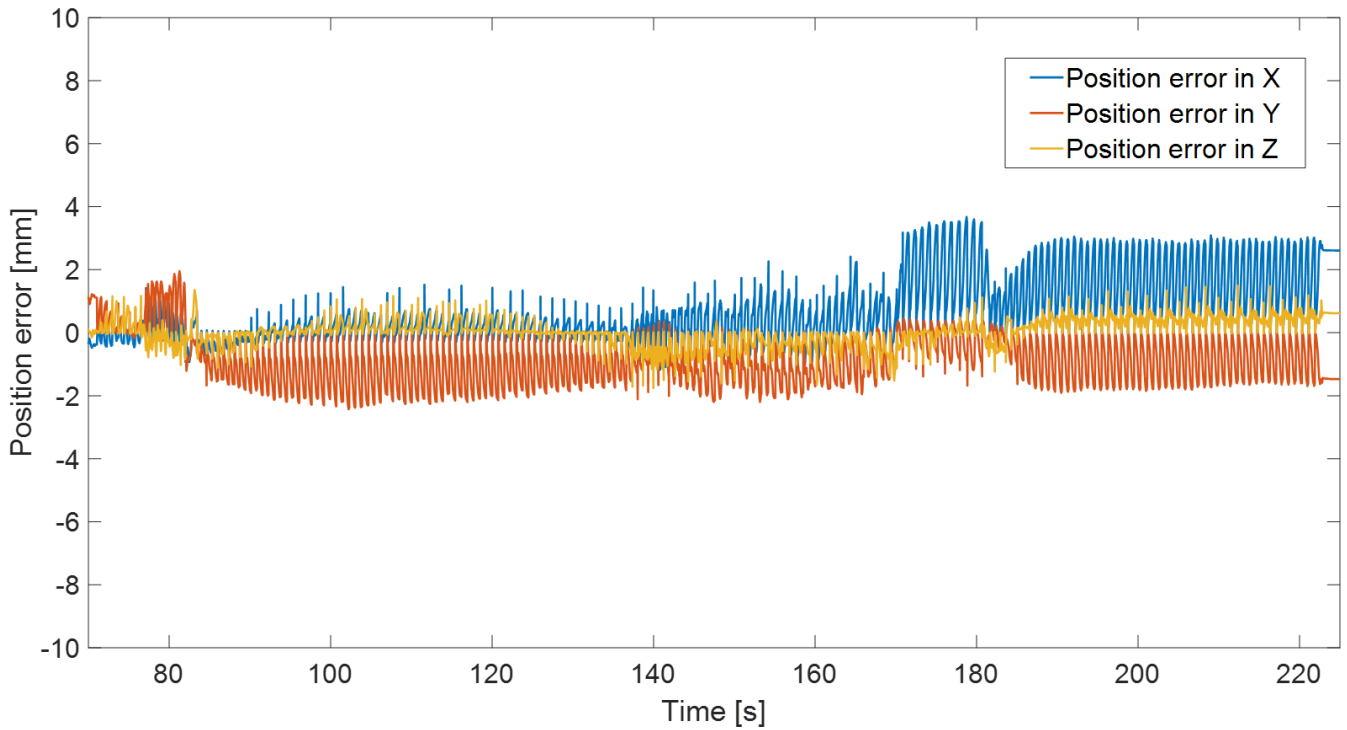


Figure 13. Second experiment (first 3-D task). Cartesian position error X_{p_e} calculated as the difference between the desired X_{p_d} and the actual X_p cartesian tool-tip position

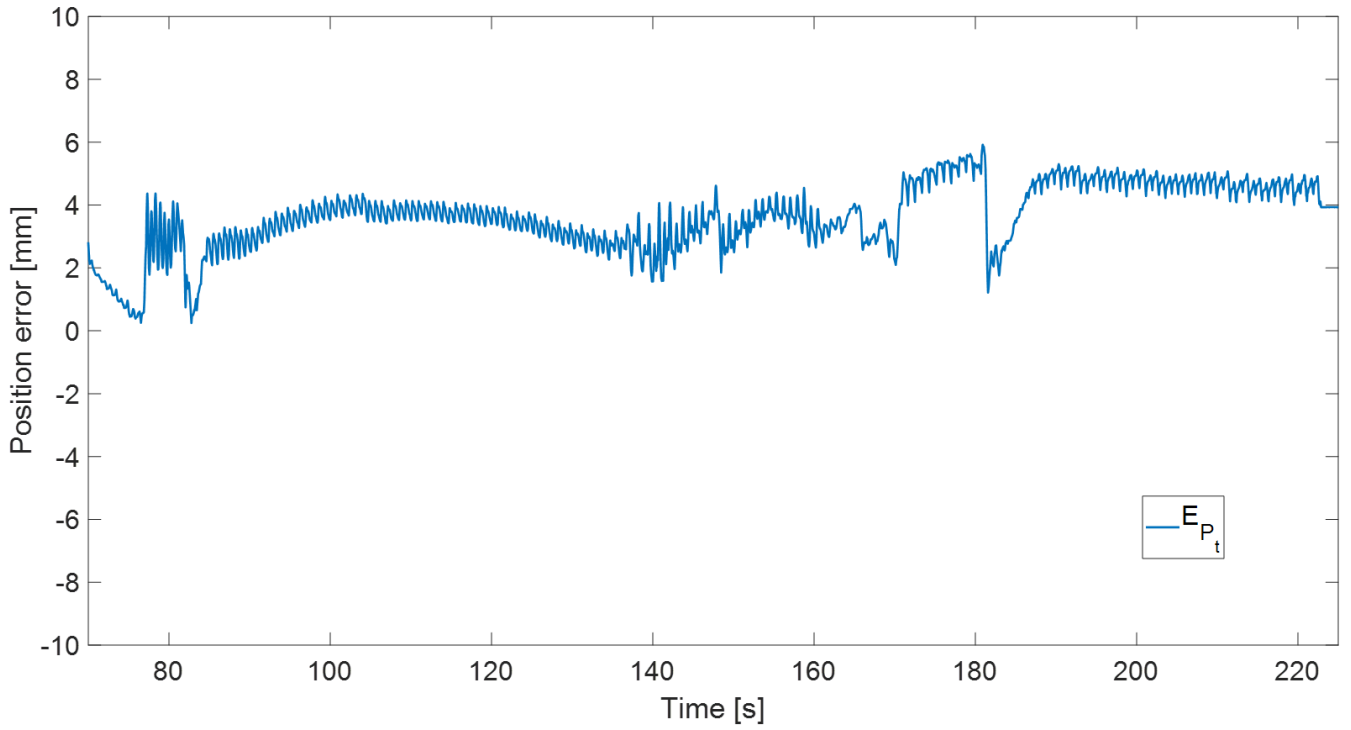


Figure 14. Second experiment (first 3-D task). RCM position error E_{P_t} calculated as the minimal distance between the trocar position P_t and the tool axis \vec{u}_c

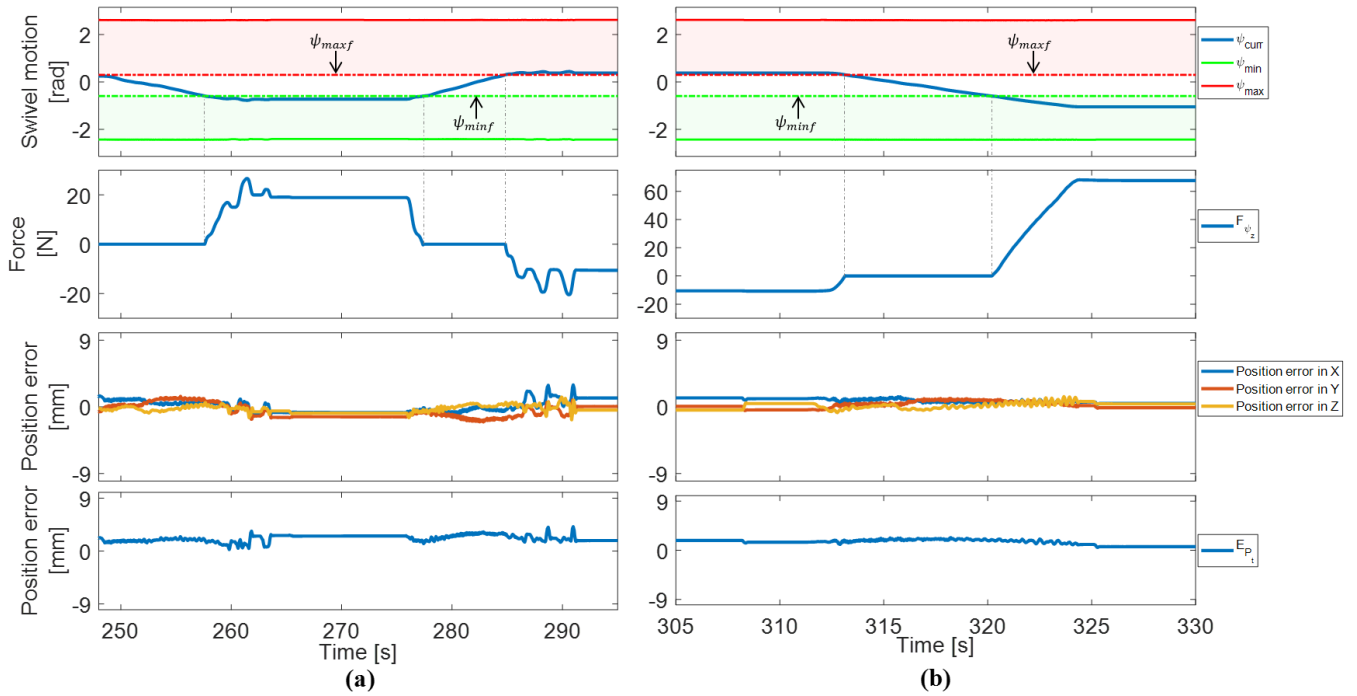


Figure 15. Second experiment. From top to bottom: swivel angle ψ behaviour, Virtual force F_{ψ_z} , Cartesian position error X_{P_e} and RCM position error E_{P_t} , respectively, obtained for the (a) second 3-D task and (b) third 3-D task

Similar to the calculation of the root-mean-square error (RMSE) of the cartesian tool-tip position $RMSE_{\lambda_{X_p}}$, the RMSE of the RCM constraint $RMSE_{\lambda_{P_t}}$ can be calculated by using:

$$RMSE_{\lambda_{P_t}} = \sqrt{\frac{\sum_{i=1}^k \|E_{P_{ti}}\|^2}{k}} \quad (17)$$

where k is the number of data points collected, $E_{p_{ti}}$ corresponds to the i^{th} RCM constraint error. The errors $RMSE_{\lambda_{p_t}}$ and $RMSE_{\lambda_{x_p}}$ were calculated for the three different tasks, as presented in Table II.

TABLE II
RMSE PERFORMANCE EVALUATION

Task	$RMSE_{\lambda_{x_p}}$ (mm)	$RMSE_{\lambda_{p_t}}$ (mm)
1	1.8	3.8
2	1.6	3.2
3	1.8	3.6

The root-mean-square error (RMSE) related to the cartesian accuracy and to the RCM constraint were calculated for each task

6. CONCLUSION

This paper proposes a collaborative control framework for robot-assisted minimally invasive general surgery, using an anthropomorphic 7-DoF torque-controlled robot. During a surgical task procedure, besides the accomplishment of the desired surgical task performed by the tool-tip, the proposed control system also guarantees that the surgical tool always goes through the trocar device placed at the incision position of the patient's body, preserving the generated RCM constraint. We have proposed an innovative null-space compliance control described by the swivel coordinates. The use of the swivel coordinates instead of the joint coordinates makes it possible to directly control the null-space configuration, since the swivel angle is a valid representation of the null-space of the Jacobian matrix J . The null-space compliance controller can be used either to constrain the swivel motion according to the joint range limits or to provide some limits given by restrictions in the robot's workspace. Moreover, the null-space controller uses the weighted generalized inverse to guarantee the dynamic consistency property. Through the proposed control approach, the robot's elbow can be manually moved without any degradation of the surgical task performance, allowing the medical staff and robot to share a common workspace during a surgical procedure. Experimental results simulating a surgical scenario were shown to validate the effectiveness of the proposed control framework.

7. ACKNOWLEDGMENT

This research was supported by the French Ministry of Research, the Department of Electronics, Information and Bioengineering of the Politecnico di Milano and the China Scholarship Council (CSC).

8. REFERENCES

- [1] C. Freschi, V. Ferrari, F. Melfi, M. Ferrari, F. Mosca, and A. Cuschieri, "Technical review of the da Vinci surgical telemanipulator," *The International Journal of Medical Robotics and Computer Assisted Surgery*, vol. 9, no. 4, pp. 396–406, 2013.
- [2] C.-H. Kuo and J. S. Dai, "Robotics for Minimally Invasive Surgery: A Historical Review from the Perspective of Kinematics," in *International Symposium on History of Machines and Mechanisms*, H.-S. Yan and M. Ceccarelli, Eds. Dordrecht: Springer Netherlands, 2009, pp. 337–354.
- [3] C.-H. Kuo, J. S. Dai, and P. Dasgupta, "Kinematic design considerations for minimally invasive surgical robots: an overview," *The International Journal of Medical Robotics and Computer Assisted Surgery*, vol. 8, no. 2, pp. 127–145, 2012.
- [4] U. Hagn et al., "The DLR MIRO: a versatile lightweight robot for surgical applications," *Industrial Robot: An International Journal*, vol. 35, no. 4, pp. 324–336, Jun. 2008.
- [5] M. Michelin, P. Poignet, and E. Dombre, "Dynamic task/posture decoupling for minimally invasive surgery motions: simulation results," in *Intelligent Robots and Systems, 2004.(IROS 2004). Proceedings. 2004 IEEE/RSJ International Conference on*, 2004, vol. 4, pp. 3625–3630.
- [6] N. Aghakhani, M. Geravand, N. Shahriari, M. Vendittelli, and G. Oriolo, "Task control with remote center of motion constraint for minimally invasive robotic surgery," in *Robotics and Automation (ICRA), 2013 IEEE International Conference on*, 2013, pp. 5807–5812.
- [7] J. Sandoval, G. Poisson, and P. Vieyres, "Improved dynamic formulation for decoupled cartesian admittance control and RCM constraint," in *Robotics and Automation (ICRA), 2016 IEEE International Conference on*, 2016, pp. 1124–1129.
- [8] H. Azimian, R. V. Patel, and M. D. Naish, "On constrained manipulation in robotics-assisted minimally invasive surgery," in *Biomedical Robotics and Biomechatronics (BioRob), 2010 3rd IEEE RAS and EMBS International Conference on*, 2010, pp. 650–655.
- [9] R. C. Locke and R. V. Patel, "Optimal remote center-of-motion location for robotics-assisted minimally-invasive surgery," in *Robotics and Automation, 2007 IEEE International Conference on*, 2007, pp. 1900–1905.
- [10] K. Fujii, A. Salerno, K. Sriskandarajah, K.-W. Kwok, K. Shetty, and G.-Z. Yang, "Gaze contingent cartesian control of a robotic arm for laparoscopic surgery," in *Intelligent Robots and Systems (IROS), 2013 IEEE/RSJ International Conference on*, 2013, pp. 3582–3589.
- [11] J. Cobb et al., "Hands-on robotic unicompartmental knee replacement," *Bone & Joint Journal*, vol. 88, no. 2, pp. 188–197, 2006.
- [12] J. G. Petersen, S. A. Bowyer, and F. R. y Baena, "Mass and friction optimization for natural motion in hands-on robotic surgery," *IEEE Transactions on Robotics*, vol. 32, no. 1, pp. 201–213, 2016.
- [13] A. A. Maciejewski and C. A. Klein, "Obstacle avoidance for kinematically redundant manipulators in dynamically varying environments," *The international journal of robotics research*, vol. 4, no. 3, pp. 109–117, 1985.
- [14] T. Yoshikawa, "Manipulability and redundancy control of robotic mechanisms," in *Robotics and Automation. Proceedings. 1985 IEEE International Conference on*, 1985, vol. 2, pp. 1004–1009.
- [15] A. Ajoudani, M. Gabiccini, N. G. Tsagarakis, and A. Bicchi, "Human-like impedance and minimum effort control for natural and efficient manipulation," in *Robotics and Automation (ICRA), 2013 IEEE International Conference on*, 2013, pp. 4499–4505.
- [16] H. Sadeghian, L. Villani, M. Keshmiri, and B. Siciliano, "Task-space control of robot manipulators with null-space compliance," *IEEE Transactions on Robotics*, vol. 30, no. 2, pp. 493–506, 2014.

- [17] R. Platt, M. Abdallah, and C. Wampler, "Multiple-priority impedance control," in Robotics and Automation (ICRA), 2011 IEEE International Conference on, 2011, pp. 6033–6038.
- [18] A. Dietrich, T. Wimbock, A. Albu-Schaffer, and G. Hirzinger, "Integration of reactive, torque-based self-collision avoidance into a task hierarchy," IEEE Transactions on Robotics, vol. 28, no. 6, pp. 1278–1293, 2012.
- [19] J. Sandoval, G. Poisson and P. Vieyres, "A New Kinematic Formulation of the RCM Constraint for Redundant Torque-Controlled Robots" in *Intelligent Robots and Systems, 2017. (IROS 2017). Proceedings. 2017 IEEE/RSJ International Conference on*, 2017. In press.
- [20] P. Dahm and F. Joubin, "Closed form solution for the inverse kinematics of a redundant robot arm." Institut für Neuroinformatik, Ruhr-Universität Bochum, April 1997.
- [21] M. Shimizu, H. Kakuya, W.-K. Yoon, K. Kitagaki, and K. Kosuge, "Analytical inverse kinematic computation for 7-DOF redundant manipulators with joint limits and its application to redundancy resolution," IEEE Transactions on Robotics, vol. 24, no. 5, pp. 1131–1142, 2008.
- [22] O. Khatib, "A unified approach for motion and force control of robot manipulators: The operational space formulation," IEEE Journal on Robotics and Automation, vol. 3, no. 1, pp. 43–53, 1987.
- [23] N. Enayati, G. Ferrigno, and E. De Momi, "Skill-based Human-robot Cooperation in Tele-operated Path Tracking", Autonomous Robots, special issue on "Learning for Human-Robot Collaboration", 2017. In press.
- [24] S. Garrido-Jurado, R. Muñoz-Salinas, F. J. Madrid-Cuevas, and M. J. Marín-Jiménez, "Automatic generation and detection of highly reliable fiducial markers under occlusion," Pattern Recognition, vol. 47, no. 6, pp. 2280–2292, 2014.
- [25] G. Schreiber, A. Stemmer, and R. Bischoff, "The fast research interface for the kuka lightweight robot," in IEEE Workshop on Innovative Robot Control Architectures for Demanding (Research) Applications How to Modify and Enhance Commercial Controllers (ICRA 2010), 2010, pp. 15–21.



*(*Corresponding author*) **Juan Sandoval** is a third year Ph.D. student on Robotics at PRISME Laboratory, University of Orléans, France. In 2012, he received his Mechatronics Engineering degree from the National University of Colombia, Bogotá, Colombia. He also earned a master's degree from the National School of Engineering ENIVL, Blois, France. His research interests include compliance control, redundancy resolution at the torque-level, and physical human-robot interaction. *Email address:* juan.sandoval-arevalo@univ-orleans.fr



Hang Su received a B.Sc. degree in Automation from Yantai University and a master degree in Control theory and control engineering at South China University of Technology, China. He is pursuing a Ph.D. degree as a member of the Neuroengineering and Medical Robotics Laboratory at Politecnico di Milano, Italy, working on technologies in tele-operation for surgical robots. His main research interests include control and instrumentation in robot assisted surgery and medical robotics. *Email address:* hang.su@polimi.it



Pierre Vieyres received his M.Sc. in Electrical engineering from University College London (UK), and his Ph.D. degree in 1990 in biomedical engineering from the University of Tours (France). In 1992, he joined the University of Orleans (France); he is currently a full time Professor in the Robotics Team of PRISME laboratory. Since 1995, he has been involved in the development of robots for the medical field and especially for tele-echography. He was the Project Manager of the OTELO European project and the national PROSIT project on robotized tele-echography. His activities focus on the development of haptic systems and collaborative robots. *Email address:* pierre.vieyres@univ-orleans.fr



Gérard Poisson is a Professor at the University of Orleans (France) and a researcher at PRISME Laboratory. He obtained the French Agrégation of Mechanics in 1980 and a Ph.D. in robotics at Orleans University in 1994. He is currently the director of the Bourges Institute of Technology (IUT) and deputy director of PRISME Laboratory.

His research interests concern various areas of robotics, including mechatronics integration, mechanical systems design and optimization for robots, perception of the environment, and Human-robot interaction. He has been involved in projects on industrial, mobile or medical robotics and has authored 100 publications. In recent years he has been specifically involved in the study and the design of dedicated devices for robotized tele-echography. *Email address:* gerard.poisson@univ-orleans.fr



Giancarlo Ferrigno, received his M.Sc. degree in electrical engineering and his Ph.D. degree in bioengineering from the Politecnico di Milano, Milan, Italy. He founded the Neuroengineering and Medical Robotics Laboratory, Politecnico di Milano, in 2008. He is currently a Full Professor of medical robotics with the Computer Science, Electronics, and Bioengineering Department (DEIB), Politecnico di Milano, where he is the Chair of the Biomedical Division. He has been the European Coordinator of three FP7-EU projects in ICT: ROBOCAST (2008–2010) and ACTIVE (2011–2015) in the field of surgical robotics, and MUNDUS (2010–2013) in the field of assistive and rehabilitative robotics. He has coauthored about 200 papers. He is a member of the ISO standard group for surgical robots and has organized several workshops in surgical robotics. **Email address:** giancarlo.ferrigno@polimi.it



Elena De Momi, received her M.Sc. and Ph.D. degrees in biomedical engineering from the Politecnico di Milano, Milan, Italy, in 2002 and 2006, respectively. She is currently an Assistant Professor in the Department of Electronics, Information, and Bioengineering, Politecnico di Milano. She is the Principal Investigator of the EDEN2020 EU project for the Politecnico di Milano. She has participated in several national and European grants in the fields of computer-assisted surgery, keyhole robotic neurosurgery, and awake robotic neurosurgery. She collaborates as an expert with the European Commission in the 7th Framework Program. Her current research interests include computer-aided surgery, medical robotics, biomechanics, and sensors. Dr. De Momi is a member of the Editorial Boards of the International Journal of Advanced Robotic Systems and the Journal of Medical Robotics Research. **Email address:**

elena.demomi@polimi.it